

Microstructural evolution and electronic properties of antiphase boundaries in elastic materials

K. H. Ahn, T. Lookman, A. Saxena, and A. R. Bishop
Theoretical Division, Los Alamos National Laboratory, Los Alamos, New Mexico 87545

The nature of the interactions governing the formation of rough fluctuating antiphase boundaries in elastic materials is shown to be short-ranged, in contrast to the long-ranged interactions responsible for smooth twin boundaries. It is demonstrated that elastic textures can generate intricate electronic inhomogeneities, as observed in many functional materials.

PACS numbers: 73.20.-r, 68.35.-p, 74.81.-g, 61.72.-y

Recent advances in imaging techniques have revealed the presence of rich elastic textures in functional materials such as colossal magnetoresistive (CMR) manganites [1, 2], ferroelectrics [3], ferroelastics [4], and shape memory alloys [5]. In particular, dark field imaging and transmission electron microscopy have been used to study the geometry of twin boundaries (TB) and antiphase boundaries (APB). Recent experiments on CMR manganites have shown metallic regions around meandering APBs within insulating charge ordered domains [2]. Understanding the formation and role of inhomogeneities, such as APB and TB, is thus central to the explanation of the electronic properties and multiphase coexistence in CMR materials.

In contrast to TBs, antiphase boundaries have not been studied well theoretically. The primary focus of the existing literature has been on aspects related to the solitary-wave profiles [4, 6]. Very little is understood about the nature of the interactions governing the formation of APBs and the apparent differences in roughness between TBs [smooth, as in Fig. 1(a)] and APBs [meandering, as in Fig. 1(b)]. It is known from critical phenomena that the smoothness or roughness of interfaces between two degenerate ground states crucially depends on the nature of the underlying interactions and is related to the existence of a phase transition and the effects of random impurities [7]. In this Letter, we demonstrate that the interactions governing the behavior of APBs are very different from those responsible for TB formation – short range versus long range – and show how these lead to the unoriented fluctuating APB profiles seen in dark field images. We perform simulations of evolving APBs, compare with TBs, and consider implications for critical phenomena. In order to show the importance of inhomogeneities, such as APB and TB, in modifying electronic properties, we perform a tight binding calculation with a Su-Schrieffer-Heeger (SSH) type model to predict the distribution of electronic density of states, which are related to the results of scanning tunneling microscope (STM) measurements. Our work thus forms the basis for predicting electronic properties from predesigned materials microstructure.

Twin boundaries separate domains related by the rota-

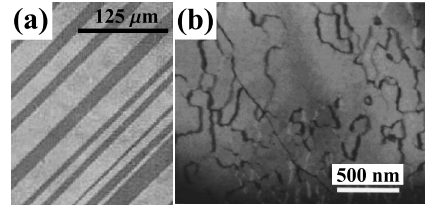


FIG. 1: (a) Image of TB: Micrograph from bulk Au-Cd. The bright and dark regions correspond to different orientations of twins. (b) Image of APB: Dark field image from bulk $\text{Nd}_{0.5}\text{Sr}_{0.5}\text{MnO}_3$. APBs are the meandering lines. [(a) and (b) by courtesy of Otsuka [5] and Mori [2], respectively.]

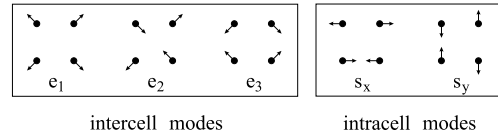


FIG. 2: Distortion modes for a square lattice in 2D with a monatomic basis [8]. For example, $s_x(\vec{i}) = [d^x(\vec{i}) - d^x(\vec{i} + (10)) + d^x(\vec{i} + (11)) - d^x(\vec{i} + (01))]/2$, where $d^x(\vec{i})$ and $d^y(\vec{i})$ represent the displacement of the atom at site \vec{i} along x and y directions respectively.

tion of crystalline axes, whereas APBs represent boundaries at which the sequence of alternating distortions, such as alternating rotational directions of oxygen octahedra in perovskite oxides, change their phase (i.e., broken translational symmetry). Although our method can be applied to two or three dimensional lattices with mono- or multiaatomic bases, we illustrate our ideas with a square lattice in two-dimensional (2D) space with a monatomic basis, for which the appropriate atomic scale distortion variables are the modes shown in Fig. 2 [8]. These modes have important advantages over displacement variables – they reflect the symmetries of the lattice and can serve as order parameters (OP) in structural phase transitions. Moreover, since the lattice distortions are decomposed into the modes at $\vec{k} = (0, 0)$ (intercell modes) and $\vec{k} = (\pi, \pi)$ (intracell modes), the approach using these modes is ideal for studying differences between long and short wavelength lattice distortions.

We consider APBs, such as the one shown in Fig. 3

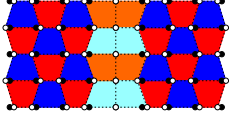


FIG. 3: (Color) An example of the atomic displacement pattern on either side of an APB. Solid and open circles represent the atomic positions for undistorted square lattice and distorted lattice, respectively. Red and blue represent the positive and negative signs of the s_x mode defined for each plaquette.

where open circles represent the distorted atomic positions, for s_x or s_y modes. The simplest energy expression yielding a ground state with either pure s_x or s_y mode lattice distortion is

$$E_{sxsy} = \sum_{\vec{i}} -\frac{D}{2} [s_x(\vec{i})^2 + s_y(\vec{i})^2] + \frac{G_1}{4} [s_x(\vec{i})^4 + s_y(\vec{i})^4] + \frac{G_2}{2} s_x(\vec{i})^2 s_y(\vec{i})^2 + \sum_{\vec{i}, n=1,2,3} \frac{C_n}{2} e_n(\vec{i})^2, \quad (1)$$

where the coefficients D , G_1 , G_2 (with $G_1 < G_2$) can be obtained from interatomic forces and C_n are the associated elastic moduli.

Since the ground state has $\vec{k} = (\pi, \pi)$ component lattice distortions, we define variables with tilde by multiplying $(-1)^{i_x+i_y}$ with all intercell/intracell/displacement variables [e.g., $\tilde{s}_x(\vec{i}) = s_x(\vec{i})(-1)^{i_x+i_y}$, $\tilde{d}_x(\vec{i}) = d_x(\vec{i})(-1)^{i_x+i_y}$]. In wavevector space, this corresponds to interchanging the $(0, 0)$ and (π, π) points. Therefore, \tilde{s}_x and \tilde{s}_y are the modes near $\vec{q} = (0, 0)$, and \tilde{e}_1 , \tilde{e}_2 , and \tilde{e}_3 are the modes near $\vec{q} = (\pi, \pi)$, where \vec{q} represents the wavevector for the variables with tilde. The constraint equations [8] in the continuum limit are $\tilde{e}_{1,3}(\vec{r}) = (\nabla_y \tilde{s}_x \pm \nabla_x \tilde{s}_y)/(2\sqrt{2})$ and $\tilde{e}_2(\vec{r}) = (\nabla_x \tilde{s}_x + \nabla_y \tilde{s}_y)/(2\sqrt{2})$. These relations show that spatial variations of *intracell* modes (\tilde{s}_x , \tilde{s}_y) always generate *intercell* modes (\tilde{e}_1 , \tilde{e}_2 , \tilde{e}_3). Therefore, intercell modes are present inside an APB at which an intracell mode with tilde changes its sign. Similar arguments apply to a TB [8] – the spatial variations of intercell modes always generate intracell modes through their constraints – and lead to a similar solitary profile for TB and APB [4, 6]. However, there exists a fundamental difference between intercell and intracell modes: In the $k \rightarrow 0$ limit, e_1 , e_2 , and e_3 are given as a first derivative of d_x and d_y , whereas in the $q \rightarrow 0$ limit, \tilde{s}_x and \tilde{s}_y are $2\tilde{d}_x$ and $2\tilde{d}_y$. Therefore, e_1 , e_2 , and e_3 are related by constraint equations, whereas \tilde{s}_x and \tilde{s}_y are not constrained by each other.

We consider the APB between the two ground states with $\tilde{s}_x(\vec{i}) = \pm\sqrt{D/G_1}$ (Fig. 3). On expanding Eq. (1) around the ground state and retaining leading order terms, we write the energy $E_{APB} = E_{APB,OP} +$

$E_{APB,NOP}$, where

$$E_{APB,NOP} = \sum_{\vec{i}, n=1,2,3} \frac{C_n}{2} \tilde{e}_n(\vec{i})^2 + \sum_{\vec{i}} \frac{D'}{2} \tilde{s}_y(\vec{i})^2 \quad (2)$$

$$E_{APB,OP} = \sum_{\vec{i}} -\frac{D}{2} \tilde{s}_x(\vec{i})^2 + \frac{G_1}{4} \tilde{s}_x(\vec{i})^4, \quad (3)$$

and $D' = D(G_2/G_1 - 1)$. The energy E_{APB} has the identical form to that for a TB with e_3 as OP [8] – a double-well potential for OP and harmonic potentials for non-OP. For both TB and APB problems, the non-OP energy terms mediate an anisotropic interaction between OPs through the constraints. The minimization of $E_{APB,NOP}$ using Lagrange multipliers leads to $E_{APB,NOP}^{\min} = \sum_{\vec{q}} \frac{1}{2} \tilde{s}_x(-\vec{q}) \tilde{U}(\vec{q}) \tilde{s}_x(\vec{q})$, where $\tilde{U}(\vec{q})$ has a q^2 leading order term with an anisotropic coefficient $\tilde{U}_2(\theta_q) = [(C_1 + C_2 + C_3) + (C_2 - C_1 - C_3) \cos 2\theta_q]/16$. When transformed into real space, the q^2 leading order term gives rise to a short range R^{-4} interaction between OP \tilde{s}_x , where R is the distance between two sites, unlike the long-range R^{-2} interaction between OP e_3 for the TB case [9, 10]. This difference in interaction range originates from the differences in the constraint equations for the two cases mentioned earlier. The short [long] range nature of the interaction between intracell [intercell] OPs significantly influences the OP correlation in the course of a phase transition, and gives rise to a rough APB [smooth TB].

The physical origin of the long-range interaction between *intercell* modes and short-range interaction between *intracell* modes lies in the difference in the symmetry operations relating the two domains separated by a TB or APB. For a TB, the sign change in OP corresponds to a change in orientation, which has no intrinsic length scale and thus gives rise to a long range interaction. For an APB, the sign change in OP signifies translation of the configuration by one atomic spacing, implying the presence of an intrinsic atomic length scale that is responsible for the fast decay of the interaction between OPs. These considerations apply to any 2D/3D lattice with mono- or multiaatomic bases. We can also expect it to be valid for the rough and fluctuating stripes suggested in high- T_C cuprates, which are examples of magnetic APBs.

We now discuss the effects of the short and long range interactions on the roughness/smoothness of the two inhomogeneities. For a TB with e_3 as OP [8, 9], the coefficient of the long range R^{-2} interaction, $U_0(\theta_k)$ [8], is nonzero except for $\theta_k = 45^\circ$ or 135° . Therefore, the boundaries along any directions except $\theta_k = 45^\circ$ or 135° cost energy proportional to the area (or volume in 3D) of the system. Therefore, any TB orientation except 45° and 135° would cost too much energy and hence disappear, which leaves only smooth TBs along 45° or 135° directions. For an APB, the OP has a short range interaction along any direction. Therefore, the energy cost for

APB is localized near the wall and proportional to the length (or area in 3D) of the wall. If we consider a continuum approximation and use the relation $\Delta = \gamma L$, where Δ represents the energy cost for the APB with length L , the problem is identical to the liquid surface model discussed in Ref. [11]. Equipartition of energy predicts that the width of the APB is roughly \sqrt{TR}/γ in 2D and $\sqrt{T}/(\pi\gamma) \times \ln(R/a)$ in 3D at finite temperature T , where a is the interatomic distance. Since the width diverges as $R \rightarrow \infty$, we expect rough antiphase boundaries [11, 12]. These arguments explain the characteristic smoothness and roughness of TBs and APBs seen in Figs. 1(a) and 1(b).

Energy minimizing simulations for TBs and APBs confirm the above conclusions. Moreover, they indicate that the long and short range interactions lead to very different correlations for intercell mode OP (TB) and intracell mode OP (APB) upon a structural phase transition. The kernel $\tilde{U}(\vec{q})$ in $E_{\text{APB,NOP}}^{\min}$ is given by

$$\begin{aligned} \tilde{U}(\vec{q}) = & \frac{C_1 + C_3}{2} T_y(\vec{q})^2 + \frac{C_2}{2} T_x(\vec{q})^2 \\ & - \frac{(C_1 + C_2 - C_3)^2 T_x(\vec{q})^2 T_y(\vec{q})^2}{4D' + 2(C_1 + C_3)T_x(\vec{q})^2 + 2C_2 T_y(\vec{q})^2}, \end{aligned} \quad (4)$$

where $T_x(\vec{q}) = \tan(q_x/2)$ and $T_y(\vec{q}) = \tan(q_y/2)$. We choose similar parameter values for both cases and use the Euler method [9] to relax the lattice starting from random initial conditions. The results, e_3 for TB and \tilde{s}_x for APB, on a 64×64 lattice with periodic boundary conditions are shown in Figs. 4 and 5, respectively, where the main panels show real space distributions and insets the k or q -space distributions. Figures 4(a) and 5(a) correspond to early stages of the relaxation, which show the characteristics of the OP distribution at high T , whereas Figs. 4(b) and 5(b) reflect the OP distributions for late stages at low T . Even at the early stage, the presence of the long range correlation between intercell OP along 45° and 135° can be identified in the main panel in Fig. 4(a), reminiscent of tweed structures in martensitic materials [9]. The k -space distribution plotted in the inset of Fig. 4(a) shows strong preference of $e_3(\vec{k})$ along 45° and 135° orientations. Such long-range correlation and anisotropy are absent for the phase of the intracell mode distortion, as shown in Fig. 5(a). The late stage of the relaxation depicted in Figs. 4(b) and 5(b) show characteristic smooth TBs and rough APBs observed in images such as Figs. 1(a) and 1(b). The TB is metastable and cannot be removed by further relaxation, unless large noise is applied. In contrast, the APB in Fig. 5(b), which is a ring due to the periodic boundary condition, shrinks and disappears upon further relaxation. Although the solitary-wave profile of the smooth APB along a certain direction is a metastable state [4], the absence of a long range interaction between the phase of intracell mode distortions prevents the relaxation of random ini-

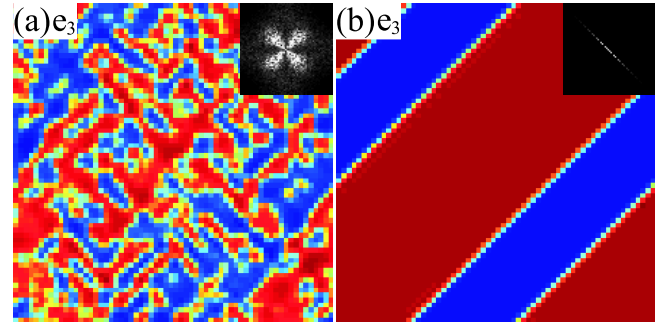


FIG. 4: (Color) $e_3(\vec{i})$ (main panels) and $|e_3(\vec{k})|$ (insets) obtained from simulation for TB: (a) early and (b) late stages of the lattice relaxation. Parameter values (see Ref. [8] for the definitions) are $A_1 = A_2 = B = 4$, $A_3 = 5$, and $F_3 = 50$. The center of the inset corresponds to $\vec{k} = 0$ and the four corners $\vec{k} = (\pm\pi, \pm\pi)$. (Dark red: 0.32, dark blue: -0.32, white color in the inset: larger than 0.2 times the maximum of $|e_3(\vec{k})|$).

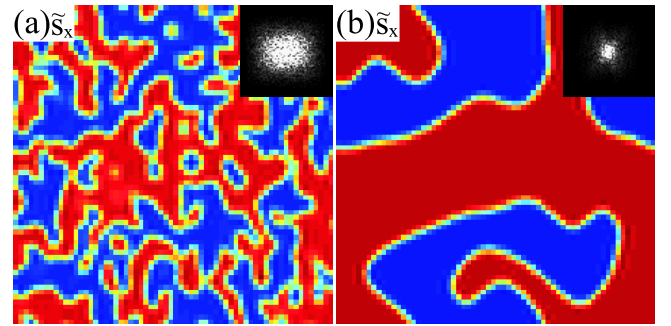


FIG. 5: (Color) $\tilde{s}_x(\vec{i})$ (main panels) and $|\tilde{s}_x(\vec{k})|$ (insets) distributions obtained from simulations for APB: (a) early and (b) late stage of the lattice relaxation. Parameter values are $C_1 = C_2 = C_3 = D' = 4$, $D = 5$, and $G_1 = 50$.

tial configuration from reaching such metastable states. This indicates that lattice defects or boundary conditions are necessary to reach the metastable solitary-wave APB configuration in materials, and influence the geometry of APBs.

To study functional electronic aspects associated with these TB and APB microstructures, we consider the modulation of electronic properties based on the following SSH electron-lattice coupling Hamiltonian,

$$H_{\text{SSH}} = \sum_{\vec{i}, a=x,y} -t_0 [1 - \alpha(d_{\vec{i}+\hat{a}}^a - d_{\vec{i}}^a)] (c_{\vec{i}}^\dagger c_{\vec{i}+\hat{a}} + c_{\vec{i}+\hat{a}}^\dagger c_{\vec{i}}), \quad (5)$$

where $c_{\vec{i}}^\dagger$ is the creation operator for an electron at \vec{i} . We use $d^x(\vec{i})$ and $d^y(\vec{i})$ obtained from our atomistic model as inputs to the SSH Hamiltonian. For $t_0 = 1$, $\alpha = 1$, and the TB and APB results shown in Figs. 4(b) and 5(b), we find all energy levels and eigenstates numerically, and calculate the local density of state (DOS) at each site and the distributions of local DOS and charge density for chosen Fermi energies (E_F), as shown in Figs. 6 and 7.

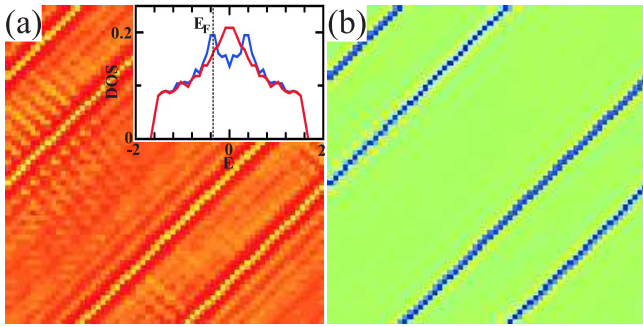


FIG. 6: (Color) Electronic properties calculated for the lattice distortion in Fig. 4(b). (a) Inset: local DOS within the domain (blue curve) and TB (red curve); main panel: spatial distribution of local DOS at E_F . (b) Corresponding charge density distribution (dark blue: 0.36, green: 0.39).

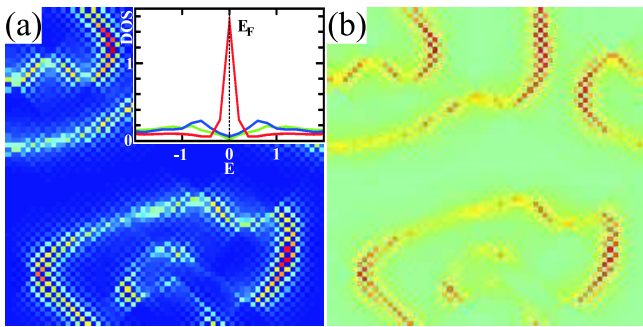


FIG. 7: (Color) Electronic properties calculated for the lattice distortion in Fig. 5(b). (a) Inset: local DOS within the domain (blue curve) and APB (red and green curves); main panel: spatial distribution of local DOS at $E_F = 0$ (dark blue: 0, dark red: 2). (b) Spatial charge density distribution for $E_F = 0.1$ (green: 0.52, dark red: 0.72).

The blue curve in the inset of Fig. 6(a) represents the local DOS within the domain of Fig. 4(b). This can be measured using direct local probes, such as STM [1, 13]. The energy difference between the two peaks is proportional to $\alpha|e_3|$. Within the TB, $|e_3|$ is small and therefore the local DOS spectral weight moves toward $E = 0$, as shown with a red curve. For E_F shown in this inset, the local DOS is smaller inside the TB than inside the domain, and the main panel of Fig. 6(a) shows the real space distribution of local DOS at this E_F . The oscillation of local DOS within the domain is related to Friedel oscillations. The charge density, which is the area in local DOS below E_F , is a constant (0.5) if $E_F = 0$. If $E_F < 0$, more electrons are depleted from the TB than the domain, as shown in Fig. 6(b).

The inset of Fig. 7(a) shows the local DOS for the APB case. Within the domain, each site has a neighbor along x axis that is closer in one direction and farther in the other (Fig. 3). Such a distortion pattern results in a V-shaped local DOS with zero DOS at $E = 0$, plotted as a blue curve in the inset of Fig. 7(a) (the small finite

value of local DOS at $E = 0$ is due to the finite energy bin size). Within the 90° APB (Fig. 3), the neighboring sites in the x -direction from the center of the APB are alternately closer or farther apart. The red line in the inset of Fig. 7(a) represents the local DOS for the sites with two farther neighbors within the APB. This has a peak near $E = 0$. The green line represents the local DOS at sites with two closer neighbors. The difference between the red and green curves emphasizes the difference that occurs in density of states due to atomistically sharp changes in microstructure as along an APB. Such changes at atomistically sharp interfaces have been seen in CMR manganites with STM (Renner *et al.* [1]). The local DOS at $E_F = 0$ is zero within the domain and finite only around the APB, as depicted in the main panel of Fig. 7(a). This means that the electronic states created by the APB dominate the low energy properties of the whole system, e.g., conductivity or specific heat. The charge density for E_F slightly higher than zero is plotted in Fig. 7(b). The results shown in Figs. 6 and 7 demonstrate that elastic inhomogeneities such as TBs and APBs can modify the local electronic properties, such as local DOS and local charge density. Although the orbital states and type of electron-lattice coupling in CMR manganites are quite different from the simple model presented here, our results suggest that the structural change within APBs and strong electron-lattice coupling may have a bearing in the creation of a metallic phase around the APB and percolative conducting paths in CMR manganites. The significance of our work is that we can now predict the electronic properties of predesigned microstructures of functional materials, which can be directly measured by STM.

In summary, we have shown that the origin of the differences between APBs and TBs lies in the nature of the short and long-range interactions between corresponding order parameters. We have studied the effects of these inhomogeneities on electronic properties.

We thank K. Otsuka and S. Mori for the images of TB and APB. This work was supported by the US DOE.

- [1] M. Uehara *et al.*, *Nature* **399**, 560 (1999); Ch. Renner *et al.*, *ibid.* **416**, 518 (2002); M. Fäh *et al.*, *Science* **285**, 1540 (1999); L. Zhang *et al.*, *ibid.* **298**, 805 (2002).
- [2] N. Fukumoto *et al.*, *Phys. Rev. B* **60**, 12963 (1999).
- [3] A. M. Abakumov *et al.*, *Phase Transition* **71**, 143 (2000).
- [4] W. Cao *et al.*, *Phys. Rev. B* **64**, 024106 (2001), W. Cao and G. R. Barsch, *Phys. Rev. B* **41**, 4334 (1990).
- [5] X. Ren and K. Otsuka, *MRS Bulletin* **27**, 115 (2002).
- [6] G. R. Barsch and J. A. Krumhansl, *Phys. Rev. Lett.* **53**, 1069 (1984).
- [7] S.-k. Ma, *Modern Theory of Critical Phenomena* (The Benjamin/Cummings Publishing Co., Reading, 1976).
- [8] K. H. Ahn *et al.*, *Phys. Rev. B* **68**, 092101 (2003).
- [9] S. R. Shenoy *et al.*, *Phys. Rev. B* **60**, R12 537 (1999), T.

Lookman *et al.*, Phys. Rev. B **67**, 024114 (2003).

- [10] In 3D, the long-rang interaction due to strain $\sim R^{-3}$.
- [11] S.-k. Ma, *Statistical Mechanics* (World Scientific Publishing Co., Philadelphia, 1985).
- [12] Discreteness of the lattice does not affect the roughness of APB in 2D, as in the boundary line problem for 2D Ising model [11]. In 3D, the Coulomb gas model of a discrete crystal surface [11] predicts the transition between rough and smooth surfaces at $T \simeq 2\gamma/\pi$.
- [13] S. H. Pan *et al.*, Nature **413**, 282 (2001).